ACS OMEGA

Open Access

http://pubs.acs.org/journal/acsodf

Article

Unveiling the Formation Pathway of Vaterite from Amorphous Calcium Carbonate Using Metadynamics Simulations

Takumi Saito, Ippei Maruyama, Yuya Suda, Atsushi Teramoto, Ryoma Kitagaki, and Takahiro Ohkubo*

Cite This: *ACS Omega* 2025, 10, 17948−17959

Read Online

ACCESS | Metrics & More | Article Recommendations | Supporting Information

ABSTRACT: Calcium carbonate is a compound that is widely distributed throughout the Earth as a natural mineral and a material produced by biological activities. The crystal structure of calcium carbonate has three polymorphs: the most thermodynamically stable calcite, followed by aragonite and vaterite. Of the three crystalline phases, the formation process and structure of the most unstable, vaterite, remain mysterious. In this study, the pathway for forming the vaterite crystal structure from amorphous $CaCO_3$ (ACC) is reproduced using well-tempered metadynamics molecular dynamics simulations. The structures sampled at multiple minima on the energy landscape are refined through first-principles calculations based on density functional theory. The sampled structures are assigned space groups and classified as calcite- and vaterite-like structures according to the arrangement of CO_3^{2-} and Ca^{2+} sheets. The initial crystal structure produced from ACC is a monoclinic crystal with Ca^{2+} sheets and CO_3^{2-} lying in the interlayer; however, it does not exhibit the 3-fold symmetry of calcite. Calcite structures with 3-fold symmetry, or orthorhombic crystals with rotated CO_3^{2-} units, as found in vaterite, can be derived from this structure. The orthorhombic structure then transitions to the more stable monoclinic form, which is likely vaterite. The understanding of phase transitions based on the diverse crystal structures of calcium carbonate revealed in this study provides a predictive view of biomineralization and carbonation reactions of cementitious materials.

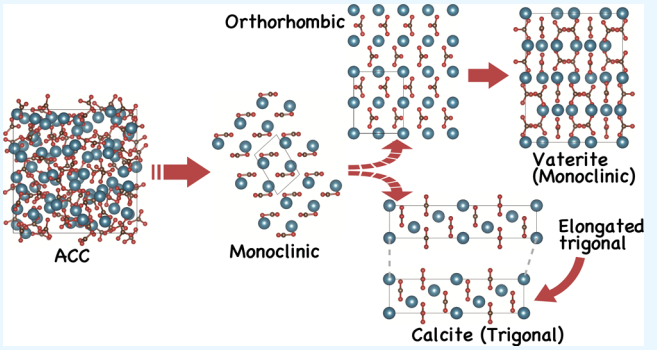

1. INTRODUCTION

The polymorphic structures of three anhydrous crystalline $CaCO_3$ forms produced via the carbonation of cementitious materials and biomineralization (calcite, aragonite, and vaterite) are well-known compounds.[1−3] Calcite is the most thermodynamically stable mineral among these phases, followed by aragonite, while vaterite is the most thermodynamically unstable.[4] Consequently, various metastable phases of vaterite give rise to a range of polymorphic structures depending on the production route and mineralization environment. Understanding the formation mechanism of carbonate minerals, including vaterite, is crucial, as it represents an important route for fixing carbon dioxide into carbonate compounds in cementitious materials[3,5,6] and biomineralization.[7−9]

The crystal structure of vaterite has been debated since its initial synthesis.[10] The structure originally proposed as the most plausible, with high symmetry, is a hexagonal model involving a helical symmetry operation, where CO_3^{2-} groups occupy interlayer positions between Ca^{2+} sheets. In this structure, CO_3^{2-} groups occupy alternating positions across Ca^{2+} sheets, forming the Kamhi model with a $P6_3/mmc$ space group (SG).[11] The lattice parameters are a = 4.13 Å and c = 8.49 Å. The CO_3^{2-} groups exhibit three-dimensional rotational freedom, while Ca^{2+} forms 6- or 7-coordinated polyhedra with oxygen atoms in CO_3^{2-}. Additionally, stacking sequences of CO_3^{2-} along the c-axis can disrupt 6-fold rotational symmetry, leading to various crystal structures with reduced symmetry.

Since 2010, theoretical studies using first-principles calculations based on density functional theory (DFT) and advanced imaging techniques, such as high-resolution transmission electron microscopy (HR-TEM), have significantly advanced understanding of vaterite crystal structures.[8,12] Light atoms such as carbon and oxygen in CO_3^{2-} can be detected using annular bright-field and atomic-resolution high-angle annular dark field (ADF) microscopy, producing clear diffraction images of microscopic regions.[12−14] Spectroscopic techniques, including Raman[15] and ^{43}Ca solid-state nuclear magnetic resonance (NMR),[16] have further refined the understanding of vaterite structures. An excellent review summarized these findings and proposed six plausible vaterite polytypes.[10] These crystal systems include trigonal and

Received: February 7, 2025
Revised: April 8, 2025
Accepted: April 11, 2025
Published: April 23, 2025

monoclinic structures with varying stacking sequences of CO_3^{2-} in the interlayer space of Ca^{2+} sheets. Recent ADF and machine-learning-aided molecular dynamics (MD) simulations have suggested plausible structures with $C2/c$ and $C2$ SGs, depending on temperature.[14]

Studies in the 2010s significantly accelerated the general understanding of vaterite structures in biologically derived or highly crystalline synthesized vaterites. However, vaterite found in cementitious materials[2,3,5,6] and biological substances[4,17−19] often exhibits low crystallinity, suggesting numerous structural possibilities, including amorphous $CaCO_3$ phases.[20−24] Minerals classified as vaterite in cementitious materials likely exhibit diverse structures, including lattice distortions, dislocations, and defects. Thermodynamically unstable vaterite is highly susceptible to environmental factors, resulting in polytypic variations during crystal growth and surface interactions in nanoscale particles.

Vaterite crystals are generally found coexisting with ACC.[17,18,25] The phase transition from ACC to vaterite is an essential pathway to understanding the formation mechanism of vaterite structures. Most ACC in natural and cementitious environments contains adsorbed water, and crystallization likely occurs due to atomic rearrangements during dehydration. This suggests that anhydrous ACC can be a precursor to crystallization.[26−28] The metastable clustering of Ca^{2+} and CO_3^{2-} in both crystalline and amorphous phases has been observed in careful X-ray diffraction experiments.[29] Although amorphous cluster formation depends on solution conditions, phase transitions from ACC to crystals proceed through complex reaction pathways.

MD simulations and DFT calculations have been extensively used to study ACC and carbonate compounds to understand their structures and phase stability.[30−32] Well-validated force field parameters for MD simulations[33] have reproduced the thermodynamic properties and structures of carbonated materials, including ACC.[34] DFT calculations employing reliable electron correlation functions have also predicted the stability of various vaterite structures.[35,36]

The phase transition from ACC to vaterite crystals requires overcoming an energy barrier of approximately 5 to 20 kJ/mol.[4] Unfortunately, equilibrium MD simulations cannot overcome this energy barrier within an accessible time scale. Additionally, the relative energy differences among vaterite polymorphs, as determined by DFT, are typically only a few kJ/mol.[35] This low rotational barrier of CO_3^{2-} in the interlayer complicates the prediction of phase transitions among vaterite polytypes using MD.

Well-tempered metadynamics MD (WTMetaD) simulations, which incorporate bias potentials to facilitate phase transitions, can reproduce phase transitions within MD time scales. To evaluate structural and free energy changes along specific reaction pathways, it is necessary to define collective variables (CVs) as bias potentials. Recent WTMetaD studies investigated $CaCO_3$ formation pathways using CVs based on atomic distances[37] and revealed multistep carbonation pathways from CO_2 to $CaCO_3$ crystalline seeds in aqueous solutions. WTMetaD simulations further explored phase transitions between $C2/c$ and $C2$ SGs, employing CVs based on CO_3^{2-} stacking distances.[14] These studies provide insight into structural changes and thermodynamic properties along specific reaction pathways.

In this study, we use WTMetaD simulations to investigate the solid−solid phase transition from anhydrous ACC to vaterite crystals. This reaction process is expected to follow more diverse pathways than those examined in previous WTMetaD studies on carbonation. Recently, the glass-to-crystal transition in oxides was successfully observed via WTMetaD, using two X-ray diffraction (XRD) peak intensities as CVs.[38] By applying the same approach, we aim to capture the diverse alignment of CO_3^{2-} during the phase transition from ACC to vaterite crystals. The vaterite structures, including transition states, will be comprehensively analyzed via WTMetaD simulations starting from the ACC structure. These structures will be used to further investigate phase stability and symmetry through DFT calculations.

2. COMPUTATIONAL METHODS

Figure 1 shows the workflow for analyzing various vaterite structures derived from WTMetaD simulations. The workflow

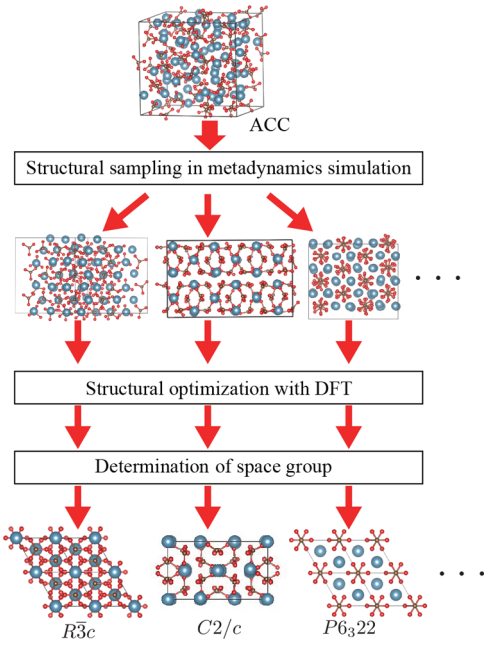

Figure 1. Workflow covering the structural sampling, refinement, and analysis of the WTMetaD simulations.

comprises structural sampling and refinement via WTMetaD and DFT calculations. The detailed computational conditions are described in later sections. The free and potential energy surfaces (FES and PES) were estimated from the WTMetaD. All structures obtained at the minima on the FES were comprehensively sampled during the WTMetaD simulations. These structures were refined through structural optimization using energy minimization by iteratively adjusting atomic coordinates with MD potentials. The optimized structures were further refined through DFT calculations. This optimization process determines the closest stable structures to those sampled in WTMetaD.

The polymorphic structures of carbonates derived from ACC are expected to exhibit numerous minima on the FES. Indeed, the FES shows a flattened bottom corresponding to indefinite structures, as demonstrated in the Results section.

The symmetry of the final optimized structures was investigated to determine their SG. The SG determination was performed using the *spglib* library[39] with a 0.5 Å distance tolerance for symmetry operations.

https://doi.org/10.1021/acsomega.5c01115
ACS Omega 2025, 10, 17948−17959

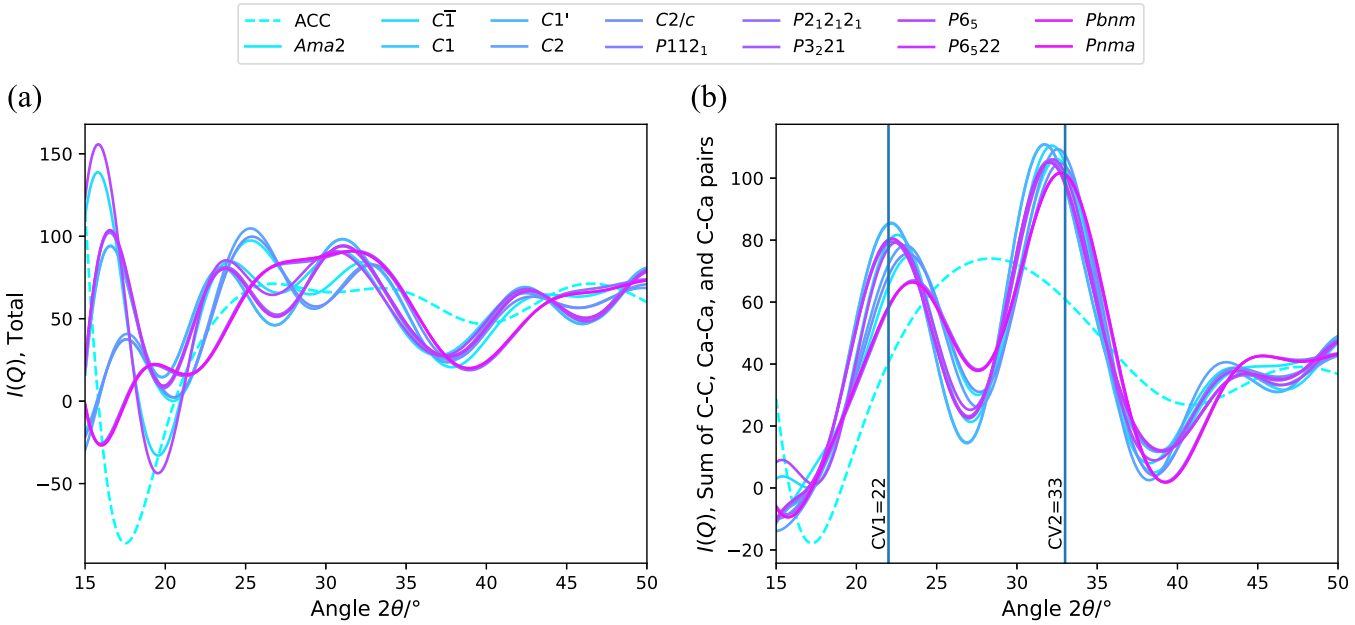

Figure 2. (a) Total and (b) partial (sum of C−C, Ca−Ca, and C−Ca) XRD patterns calculated from the proposed vaterite crystal structures[32,36,44,45] and ACC. Two structures with different *C*1 SGs are labeled with *C*1 and *C*1′. Since the five ACCs show the same line, the data of one representative ACC is shown.

VESTA[40] was used to visualize the crystal structure in this study.

2.1. WTMetaD Simulation. An extensive search space related to vaterite phases was comprehensively explored using WTMetaD simulations with two CVs. A history-dependent external potential $V(\boldsymbol{s},t)$ derived from the CVs $\boldsymbol{s}(t)$ at time t is expressed in the WTMetaD simulations as follows:[41]

$$V(\boldsymbol{s}, t) = V(\boldsymbol{s}, t-1) + G(\boldsymbol{s}, \boldsymbol{s}(t)) \exp\left[-\frac{1}{\gamma - 1}\beta V(\boldsymbol{s}, t-1)\right] \quad (1)$$

where γ and $\beta = \frac{1}{k_B T}$ are the controllable bias factor and the inverse thermal energy with Boltzmann constant k_B. $G(\boldsymbol{s},\boldsymbol{s}(t))$ is the biasing potential with the Gaussian form of $\boldsymbol{s}$ with height ω and width σ_ω

$$G(\boldsymbol{s}, \boldsymbol{s}(t)) = \omega \exp\left[-\sum_{\alpha=1}^{N_{CV}} \frac{(\boldsymbol{s}_\alpha(t) - \boldsymbol{s}_\alpha(k\tau))^2}{2{\sigma_\alpha}^2}\right] \quad (2)$$

The bias potential is deposited to CVs at every $k\tau$, where k is an integer and τ is the interval. In the WTMetaD simulation, the time interval $V(\boldsymbol{s},t)$ is updated as the simulation progresses, and the intermediate structures in the search phase space are explored while avoiding revisited $\boldsymbol{s}$. $V(\boldsymbol{s},\boldsymbol{s}(t))$ in the WTMetaD simulation is scaled by γ, meaning that the increment of $V(\boldsymbol{s},t)$ becomes gradually smaller over time with well-parametrized γ.

Two CVs derived from two peak intensities, $I(Q)$, on the XRD diffraction pattern were chosen to focus on the symmetry of the unit cell to allow for an extensive search not restricted to a specific reaction pathway. The intensity of the XRD pattern was computed from atomic coordinates using the Debye formula[42] with the Lorch function[43] to eliminate artifacts from the finite lattice size, considering atomic pairs:

$$I(Q) = \frac{1}{N}\sum_{i=1}^{N}\sum_{j=1}^{N} f_i(Q) f_j(Q) \frac{\sin(Qr_{ij})}{Qr_{ij}} \cdot \frac{\sin(\pi r_{ij}/R_c)}{\pi r_{ij}/R_c} \quad (3)$$

where r_{ij} is the distance between atoms i and j, and Q is the magnitude of the scattering vector ($Q = \frac{4\pi}{\lambda}\sin(\theta)$, where λ is the X-ray wavelength of Cu-K_α radiation (1.5406 Å), and θ is the Bragg angle). R_c is the upper limit for the r_{ij} calculation.

The total $I(Q)$ and the sum of partial $I(Q)$ from C−C, Ca−Ca, and C−Ca pairs were calculated from the crystalline structures of available vaterite crystals[32,36,44,45] and ACC, as shown in Figure 2a,b. ACC structures were constructed using the melt-quenching method following a previous study.[30] Five ACC structures, created starting from different initial configurations with 360 atoms (72 $CaCO_3$), were independently prepared to evaluate the statistical error. It was confirmed that the line shape of the FES derived from WTMetaD simulations was independent of the initial ACC structures. Characteristic peaks representing vaterite crystals at 22° and 33° (CV1 and CV2 in Figure 2) in partial $I(Q)$ were chosen as the CVs in the WTMetaD simulations. Strong intensities at these peaks are common features of experimentally reported vaterite crystals.

The large-scale atomic/molecular massively parallel simulator (LAMMPS)[46] integrated with the Plumed package (version 2.7.5)[47] was used to perform the WTMetaD simulations. The force field parameters and functionals were adopted rigid-model developed from Raiteri et al. (rigid model).[48] This is an extension of their previous study[33] and accurately reproduces thermodynamic properties such as solubility and hydration-free energy.

A polarizable force field based on the AMOEBA model has been developed for calcium carbonate in water.[49] Using both force field parameters, the lattice constants and atomic positions of calcite, aragonite, and vaterite ($P3_221$ SG) crystals were optimized via energy minimization. The experimental lattice constants of calcite and aragonite were reproduced

https://doi.org/10.1021/acsomega.5c01115
ACS Omega 2025, 10, 17948−17959

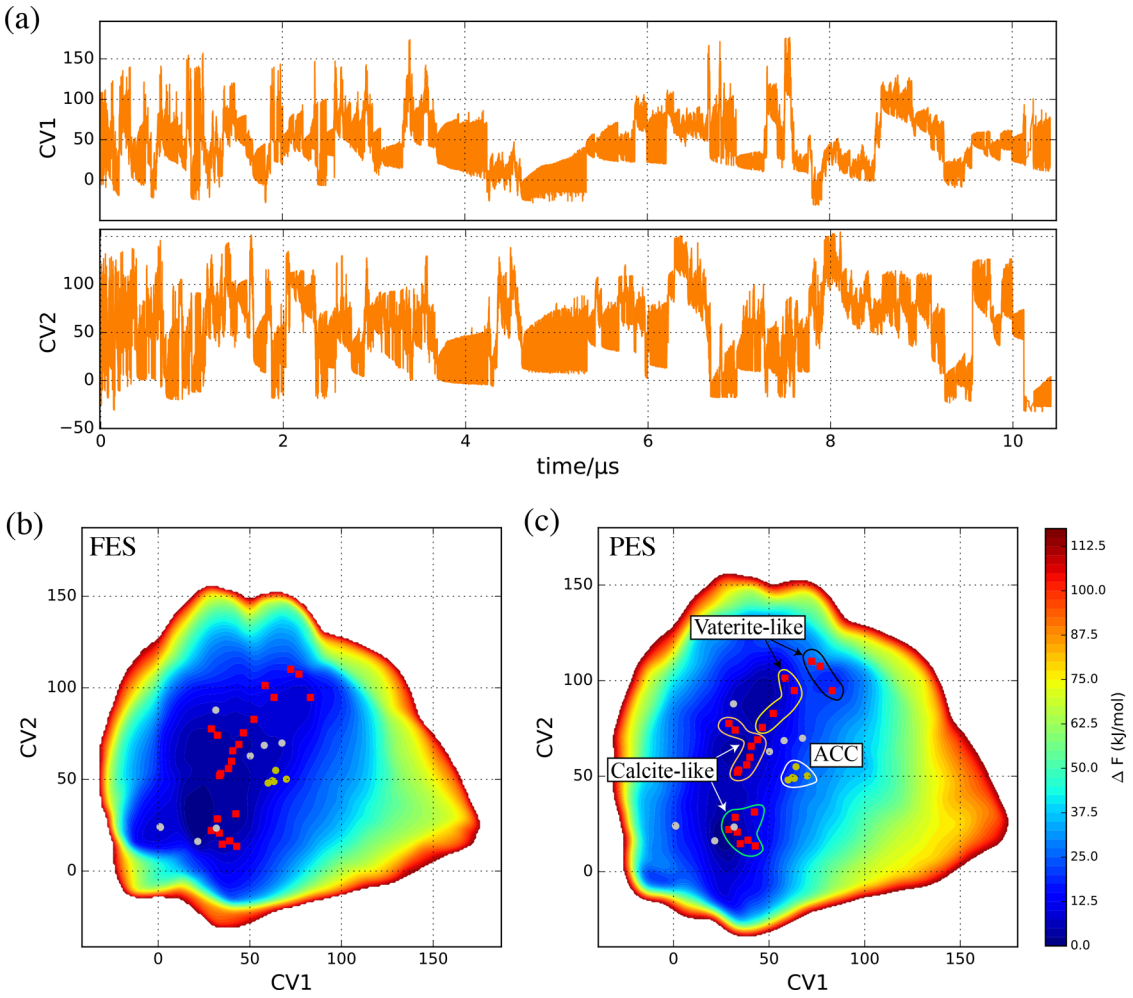

Figure 3. (a) Time evolution of two CVs obtained from metadynamics simulations; (b) and (c) FES and PES derived from the two CVs at 10.4 μs. The markers in (b) and (c) are minima points of sample structures. Sampling points of the structures attributed to P_1 and other space groups are indicated by gray circles and red squares on the FES and PES. Sampling points classified as calcite-like and vaterite-like based on structural characteristics are surrounded by colored lines in (c).

within 2% by both force fields. However, discrepancies of approximately 30% were observed in the lattice constants of vaterite ($P3_221$ SG) derived from the AMOEBA model. This discrepancy may be attributed to overfitting, as the model was specifically designed to reproduce the hydration energy of the calcite-water system. In contrast, the lattice constants obtained from the rigid model exhibited good agreement with experimental data for all three carbonate crystals.

Although reactive force fields[37,50] and machine-learning potentials could be considered as alternatives, their high computational cost for long simulation times, which are necessary to sample diverse structures, renders them impractical. Moreover, machine-learning potentials often produce inaccurate results for configurations that were not included in the training data set. For example, an equilibrium glass melt structure starting from a completely random atomic configuration cannot be accurately generated by machine-learning potentials.[51] Preparing exhaustive training data to cover all possible solid−solid phase transitions is not feasible. Overall, the rigid model was deemed the most appropriate choice among the available force fields for this study, which focuses on the phase transition from amorphous calcium carbonate (ACC) to vaterite.

The WTMetaD simulation started from an ACC structure with a 2.649 g/cm^3 density. The simulation temperature was set to 800 K to accelerate the reaction, which is below the melting point of stable calcite (1600 K) and aragonite (1098 K). WTMetaD was performed in an isothermal−isobaric (NPT) ensemble controlled by the Nosé−Hoover method[52] at 1 atm with a 1 fs time step of up to 10.4 μs.

The deposition time of WTMetaD in eq 2 was set to 1 ps, and $V(s,t)$ was updated every 1 ps. The setting of σ was empirically determined as σ = 3 following previous work.[53] The γ and ω were set to 200 and 5 kcal/mol, which sufficiently induced the phase transitions at the desired frequency.

Constraints on the maximum ratio of cell lengths (b/a, c/a, and c/b) were imposed during the WTMetaD simulations to avoid symmetry collapse due to extremely low-dimensional structures (e.g., needle- or plate-like unit cells) caused by tilting. The limits on variable cell lengths were determined from equilibrium MD at 1000 K in the NPT ensemble, which is higher than the temperature used for the WTMetaD in this study. From the lower and upper bounds of cell deformation, the constraints on the maximum cell length ratios were set to $1.12 \le b/a \le 1.28$, $0.74 \le c/a \le 0.88$, and $0.60 \le c/b \le 0.75$.

2.2. Structural Relaxation. The energy of the sampled structures was minimized by adjusting atomic coordinates to

https://doi.org/10.1021/acsomega.5c01115
ACS Omega 2025, 10, 17948−17959

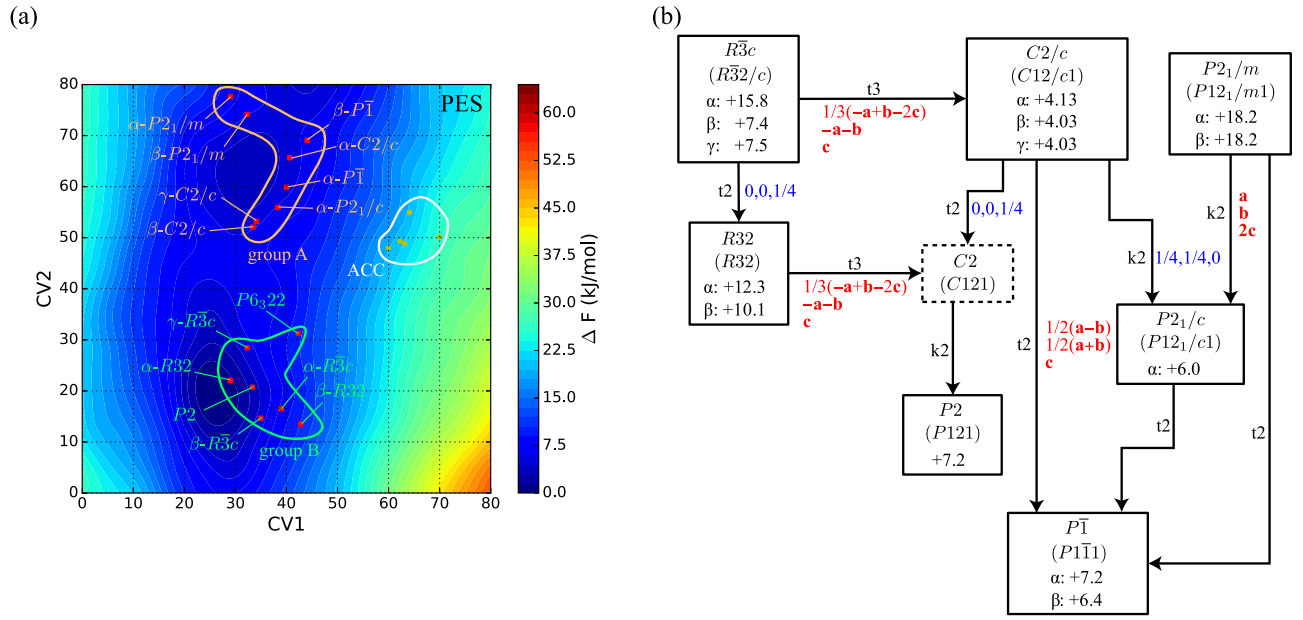

Figure 4. (a) Sampled points on PES as calcite-like structures. The sampled points are classified as monoclinic (group A) and mainly trigonal (group B) with SG labels. Five points corresponding to CVs of ACC are enclosed by a white line. (b) Subgroup graph for SGs derived from the sampled structures in (a). *t* and *k* on connected lines indicate reducing symmetry operations with *translationengleiche* and *klassengleiche*. The indices of *t* and *k* indicate the number of reducing symmetry operations.

satisfy a tolerance of 1×10^{-8} kcal/mol using MD potentials. Subsequently, structural optimization was further investigated using DFT calculations with the Vienna Ab initio Simulation Package (VASP).[54−56] The projector-augmented wave (PAW) method was used to describe the electron−core interactions. The modified Perdew−Burke−Ernzerhof GGA for solids (PBEsol),[57] which accurately reproduces the experimental enthalpy of vaterites,[35] was adopted for the DFT calculations. The atomic positions and cell lengths were optimized to achieve a convergence of 10^{-3} eV/Å for the force components acting on each atom.

3. RESULTS

3.1. Metadynamics Simulation. Time-dependent CVs provided information on the repeatable phase transition between ACC and crystalline phases, as observed in Figure 3a. Structures generated from various combinations of two CVs were sampled during the WTMetaD simulations. The frequency of phase transitions decreased in the latter half of the simulation, confirming that introducing the bias factor reduces the bias deposition rate.

Figure 3b,c show the FES and PES landscapes for the reaction between ACC and other phases as a function of two collective variables (CV1 and CV2). CV1 and CV2 correspond to $I(Q)$, as shown in Figure 2. The color scale on the right indicates the free energy difference ΔF in kJ/mol per $CaCO_3$, with blue and red corresponding to lower and higher energy states, respectively. The convergence of the FES profile was confirmed by comparing FES from 9 to 10.4 μs, as shown in Figure S1. A movie of the time-evolving FES during WTMetaD is provided in the Supporting Information. The two FES profiles at 9 and 10.4 μs were identical. The emergence of new structures was completed within 4 μs, as summarized in Table S3, where the time of first emergence and subsequent transitions were tabulated along with the SG and energy. Therefore, the WTMetaD simulation for 10.4 μs reached convergence, allowing for the analysis of energetic and structural information for the various structures.

The FES reveals the presence of multiple energy minima, corresponding to metastable states separated by minor energy barriers in the central region, as shown in Figure 3c. Structures at all local minima on the FES were sampled for subsequent structural analyses. A total of 30 structures were sampled as metastable states, as indicated by gray circles and red square-filled markers in Figure 3c. Sampling points with red square-filled markers were attributed to structures with SGs other than *P*1. These structures are shown in Figures S3−S8 along with their SGs. Structures attributed to the *P*1 SG, displayed as gray circles, were found across various CVs. To organize the symmetry-based pathway, structures with the *P*1 SG are not considered in the later discussion. Crystalline structures with SGs other than *P*1 were further classified as "calcite-like" and "vaterite-like" structures based on the alignment of CO_3^{2-} and Ca^{2+}, as labeled in Figure 3c. The calcite-like structures consist of Ca^{2+} sheets with CO_3^{2-} lying parallel to Ca^{2+} sheets in the interlayer. In contrast, CO_3^{2-} in vaterite-like structures are arranged with rotational symmetry in the interlayer, forming various stacking structures.

Five points derived from ACC structures were also plotted on the FES and PES. They exhibit higher energy than the crystalline sampled points, suggesting that their thermodynamic stability is lower than that of crystalline structures. The calcite-like structures were scattered in the region of 20 < CV 1 < 50 and 10 < CV 2 < 80. In contrast, vaterite-like structures were found in the region of 40 < CV 1 < 90 and 70 < CV 2 < 120. To organize the phase transitions in terms of structural symmetry, the sampled structures are discussed separately as calcite-like and vaterite-like in the following sections.

3.2. Calcite-like Structures. Figure 4a illustrates the PES for the area 0 < CV1 < 80 and 0 < CV2 < 80, where all sampled points were assigned to calcite-like structures. The PES forms a broad flat region for CV1 between 20 and 40,

https://doi.org/10.1021/acsomega.5c01115
ACS Omega 2025, 10, 17948−17959

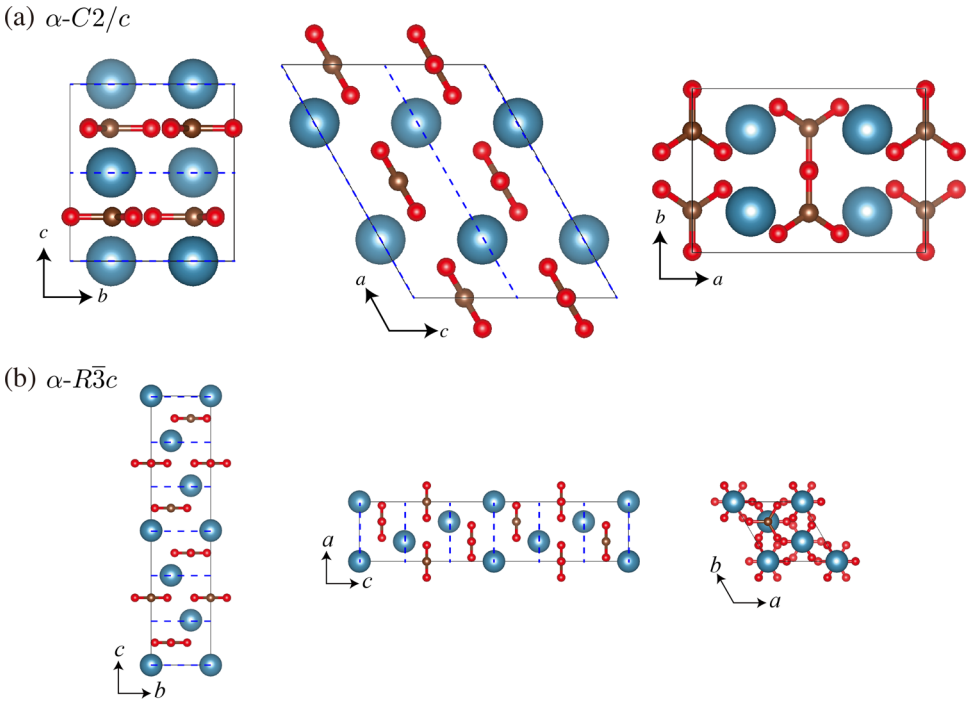

Figure 5. Examples of crystalline structures detected in groups A and B. CO_3^{2-} are aligned in the stacking direction in the Ca sheets displayed with blue dotted line: (a) monoclinic and (b) trigonal crystal systems. Ca, C, and O atoms are drawn by silver, brown, and red spheres.

suggesting that numerous metastable structures are thermodynamically equivalent. Initial CVs derived from five different ACC configurations are also shown around (CV1, CV2) = (62, 50). In the 0 < CV1 < 80 and 0 < CV2 < 80 region, structures at the multiple minima are sampled for 15 points, each labeled with a specific SG. Structures with the same SG but different lattice constants are distinguished through prefixing with Greek letters in order of their emergence. Tables S2 and S3 summarize the lattice constants and emergence times for all detected structures.

The sampled calcite-like structures were classified into two groups, labeled as "A" and "B", as shown in Figure 4a. Selected crystalline structures in groups A and B are shown in Figure 5, corresponding to $C2/c$ and $R\bar{3}c$ SGs, respectively, with blue lines representing Ca^{2+} sheets. The monoclinic structures in group A exhibit 2-fold screw, mirror, and glide operations. All Ca^{2+} sheets are stacked perpendicular to the CO_3^{2-} layers, as shown in Figure 5. The disordering of the 2-fold screw leads to the $P\bar{1}$ SG, which exhibits imperfect CO_3^{2-} alignment, as seen in Figures S3 and S4. The CO_3^{2-} with 3-fold symmetry can align alternatively through $\pi/3$ rotation, producing screw or glide symmetry parallel to the Ca^{2+} sheet. Structures in group B, with 3-fold symmetry in the stacking direction of Ca^{2+} sheets, are shown in Figure 5b. Although the WTMetaD simulation focused on the XRD peak intensities of vaterite structures, calcite-like structures with 3-fold symmetry were detected due to their thermodynamic stability. Structures similar to the high-temperature phase of aragonite with the $P6_322$ SG were also found in group B.[58] This study used $I(Q)$ of vaterite crystals to observe the pathway from ACC to vaterite. Therefore, it is likely that the intermediate states for the transition to aragonite were not fully sampled. Consequently, the discussion of the transition from ACC to aragonite was limited in this study.

The c-axis length (18.20−18.66 Å) of the sampled $R\bar{3}/c$ SG with 6 Ca^{2+} sheets, as indicated in Table S2, is longer than that of stable calcite crystals (17.6 Å).[59] A similar calcite structure with a longer c-axis is observed during the phase transition to $R\bar{3}/m$ at elevated temperatures.[60] Structures with 3-fold screws in the stacking direction of Ca^{2+} sheets and disordering of the 3-fold symmetry also resulted in different structures with $R32$ and $P2$ SGs.

The energies of the detected calcite-like structures, derived from DFT calculations, are shown in Figure 6, with the relative value for the calcite crystal.[59] Note that the energy of calcite crystals is evaluated after structural optimization through DFT calculations. The three structures α-, β-, and γ-$C2/c$ have similar energies around 4 kJ/mol. A loss of translational

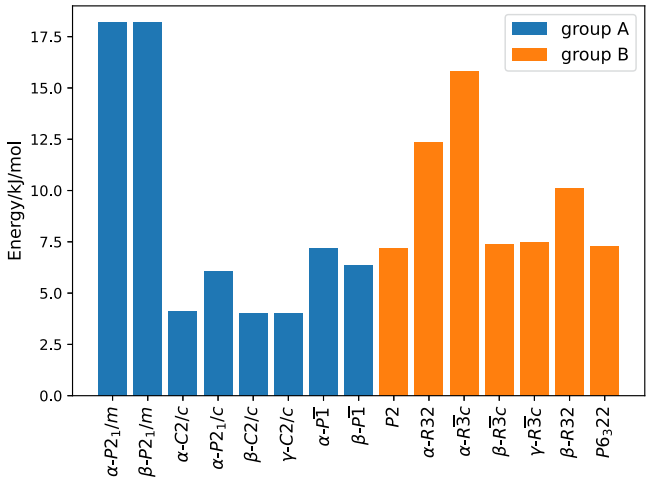

Figure 6. Energies of calcite-like structures sampled from WTMetaD simulations for the relative value of the calcite crystal.

https://doi.org/10.1021/acsomega.5c01115
ACS Omega 2025, 10, 17948−17959

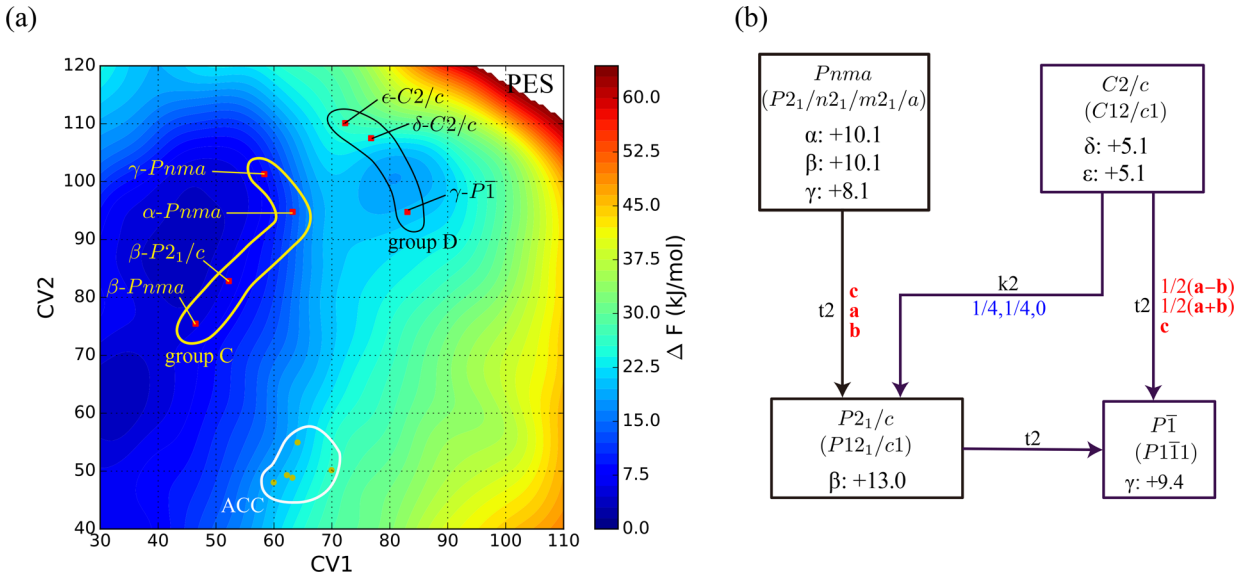

Figure 7. (a) Sampled points on PES as vaterite-like structures. The sampled points are classified into orthorhombic (group C) and monoclinic and triclinic (group D) systems, shown with SG labels. Five points corresponding to ACC CVs are enclosed by a white line. (b) Subgroup graph for SGs derived from the sampled structures in (a). Notations on each line connecting space groups indicate reducing symmetry, as described in Figure 4.

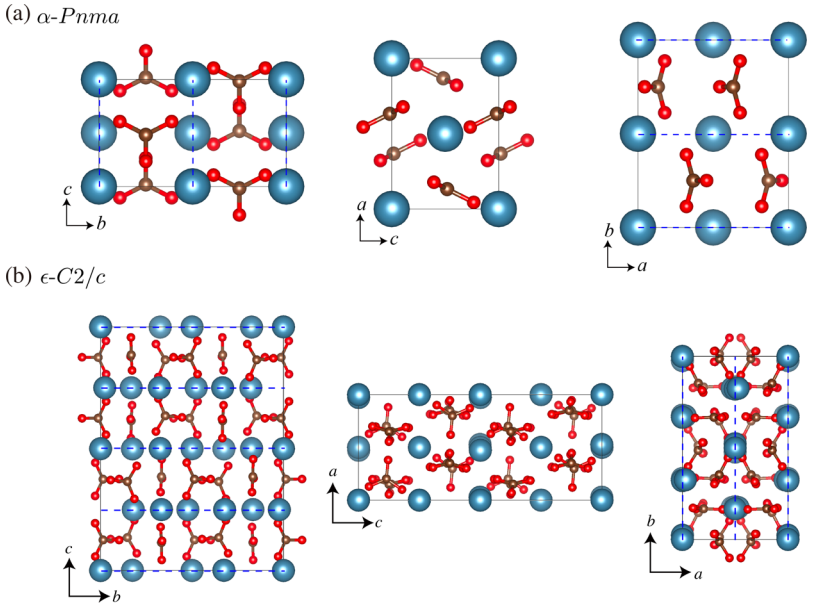

Figure 8. Selected structures of vaterite-like crystals derived from the WTMetaD simulation. Ca, C, and O atoms are drawn by silver, brown, and red spheres. Ca^{2+} sheets are indicated by blue dotted lines. (a) Orthorhombic in group C and (b) monoclinic in group D.

symmetry from the $C2/c$ SG leads to the $P2_1/c$ SG, with a slightly higher energy of 2 kJ/mol.

Structures with 3-fold symmetry have energies ranging from 7 to 16 kJ/mol, depending on cell dimensions. Two SGs ($R32$ and $R\bar{3}c$) are associated with the $\pi/3$ rotation of CO_3^{2-}. This rotation has a very low energy barrier, as demonstrated in MD simulations.[61] These structures can be identified as metastable calcite structures, with a slightly shorter a-axis and longer c-axis (~0.14 and 1 Å, respectively) than stable calcite crystals, as shown in Table S2. The resulting density is about 2% lower than that of calcite crystals but higher than that of vaterite crystals (~2.54 g/cm^3). Notably, a calcite structure perfectly matching experimental data did not emerge, likely due to the use of XRD CVs tailored for vaterite crystals.

Structural changes during phase transitions entail symmetry generation or destruction. The subgroup graph of SGs for calcite-like structures derived from the WTMetaD simulations is visualized in Figure 4b. SGs, accompanied by DFT-derived energies, are connected by arrows indicating decreasing symmetry, as referenced in International Tables A1.[62] The construction of the subgroup graph can be also confirmed via "Bilbao Crystallographic Server".[63−65] The labels t and k on the connecting lines refer to *translationengleiche* and *klassengleiche*, where t indicates reduced point group operations while preserving translational symmetry, and k refers to reduced translational symmetry while maintaining point group operations. The attached numbers indicate the degree of symmetry reduction. Blue and red text indicating the origin

https://doi.org/10.1021/acsomega.5c01115
ACS Omega 2025, 10, 17948−17959

shift and the new lattice vectors for the enlarged unit cell have been added to the arrows.

Trigonal $R\bar{3}c$ and $R32$ SGs are linked by t_2, and both can transition to monoclinic by t_3. The $C2$ SG, surrounded by a dotted line in Figure 4b, was not detected in WTMetaD simulations but likely represents an intermediate state in the transition from $R32$ SG to $P2_1/m$ SG. $P2_1/m$ and $P2_1/c$ SGs cannot directly originate from the trigonal system; they likely emerge from ACC through incremental symmetry changes via $C2$ systems.

Based on the PES in Figure 4a, two possible routes from ACC are suggested: $P\bar{1}$, $C2/c$, and $P21/c$ (route 1a) or $R\bar{3}c$ and $R32$ (route 1b), both close to CVs for ACC. Considering phase transitions with a gradual increase in symmetry, transitions from ACC to group B structures via group A structures along route 1b appear predominant. The CV values of vaterite crystals are (CV1, CV2) = (80, 100), which means they are positioned in the upper right region relative to group A. Therefore, $P\bar{1}$, $C2/c$, and $P21/c$ SGs, close to the CVs of vaterite crystals, may represent transition states leading to vaterite structures.

3.3. Vaterite-like Structures. Figure 7 shows the PES with sampled points in the region 30 < CV1 < 110 and 40 < CV2 < 120. The sampled points were assigned SGs via structural optimization using DFT calculations. The determined structures are classified into two groups (C and D) according to the sampled regions. Group C exhibits lower ΔF, which is almost at the same level as those of groups A and B for calcite-like structures. Meanwhile, structures with ΔF values 10 to 20 kJ/mol higher are assigned to group D, which emerged as the closest points to the CVs of vaterite crystals. Examples of the orthorhombic and monoclinic structures in groups C and D are shown in Figure 8.

In the orthorhombic structures, CO_3^{2-} are arranged with tilts relative to each other along the stacking direction of Ca^{2+} sheets. The crystal structure organized by this CO_3^{2-} alignment resembles the orthorhombic structure derived from XRD patterns.[44,45] Note that the *Pbnm* SG reported by Meyer is equivalent to *Pnma* by axis conversion. Several authors have also performed DFT calculations based on these experimental results for orthorhombic systems.[32,35,36]

The monoclinic structures emerging in group D exhibit CO_3^{2-} rotation associated with the stacking sequence in Ca^{2+} sheets, as shown in Figure 8b. The structure with $C2/c$ SG is consistent with the four-layer structure determined by electron diffraction and ADF[13,14,66] of vaterite. A variety of structures involving CO_3^{2-} rotation with different alignments in the stacking sequence of Ca^{2+} sheets have been proposed by introducing rotational disorder in the hexagonal model (P_{6_3}/mmc).[11] These structures with monoclinic systems are attributed to different SGs and diversified by combinations of hexagonal arrangements through $\pi/3$ or $2\pi/3$ rotations.[14] Although only $C2/c$ SG was found in this simulation, it is reasonable to consider that the low rotational barrier in the interlayer produces metastable polymorphs of other monoclinic crystals. These polymorphs were likely undetectable in WTMetaD simulations due to the very flat potential surface at high temperatures.

The energies of the sampled vaterite-like structures are plotted relative to the calcite structure in Figure 9. The results calculated from the proposed vaterite crystal structures[32] are also shown in Figure 9. The structures with $P2_1/c$ and *Pnma*

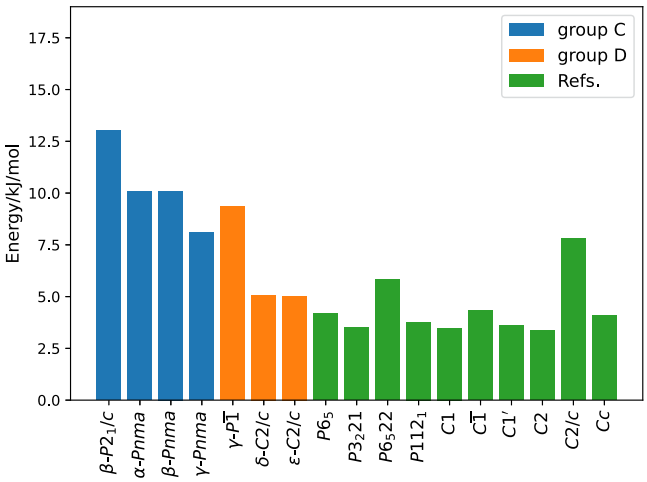

Figure 9. Energy differences of vaterite-like structures sampled during the WTMetaD simulations and vaterite crystals from previous studies.[32] The relative energies of calcite crystal are also plotted.

SGs in group C have higher energies of about 5 and 7 kJ/mol than the structure with $C2/c$ SG, which is a probable vaterite structure. The $P\bar{1}$ structure has a higher energy of approximately 10 kJ/mol relative to calcite. These structures are attributed to metastable states during vaterite formation from ACC.

The energies obtained from orthorhombic systems in group C are higher than those from monoclinic structures in group D, suggesting that orthorhombic systems represent transition states or nonviable structures. Indeed, the density of these structures is higher (~2.70 g/cm^3) than that of experimental vaterite data (~2.66 g/cm^3). The $P2_1/c$ SG found in group C represents a slightly tilted structure compared to orthorhombic cells. The CO_3^{2-} arrangement in the interlayer is similar to other *Pnma* crystal structures.

The subgroup graph shown in Figure 7b represents phase transitions based on symmetry. The *Pnma* SG of the orthorhombic structure can transform to $P2_1/c$ by reducing point group symmetry operations while retaining translational symmetry (t_2). This structure connects to the final $C2/c$ SG structure, either directly or via $P\bar{1}$.

4. DISCUSSION

The pathway for generating vaterite crystals from ACC was examined from a crystallographic perspective. A schematic of the phase transition is depicted in Figure 10.

The first step in symmetry generation from ACC involves the formation of Ca^{2+} sheets with CO_3^{2-} lying in the interlayer, primarily resulting in the monoclinic crystalline systems categorized as group A in Figure 4. This structural change appeared at the initial stage of the WTMetaD simulations, around 500 ns, as shown in Table S3 and a movie of the time-varying FES of crystal structures in the Supporting Information. These structures can be considered embryos for phase transitions to either vaterite or the most stable calcite. Since XRD peak intensities of vaterite crystals were used as CVs in the WTMetaD simulations, structures perfectly consistent with calcite crystals did not emerge in group B of Figure 4. However, several energetically unstable calcite-like structures with elongated cell dimensions along the 3-fold symmetry axis were detected. These structures may serve as precursor crystals for stable calcite with $R\bar{3}c$ SG. Such

https://doi.org/10.1021/acsomega.5c01115
ACS Omega 2025, 10, 17948−17959

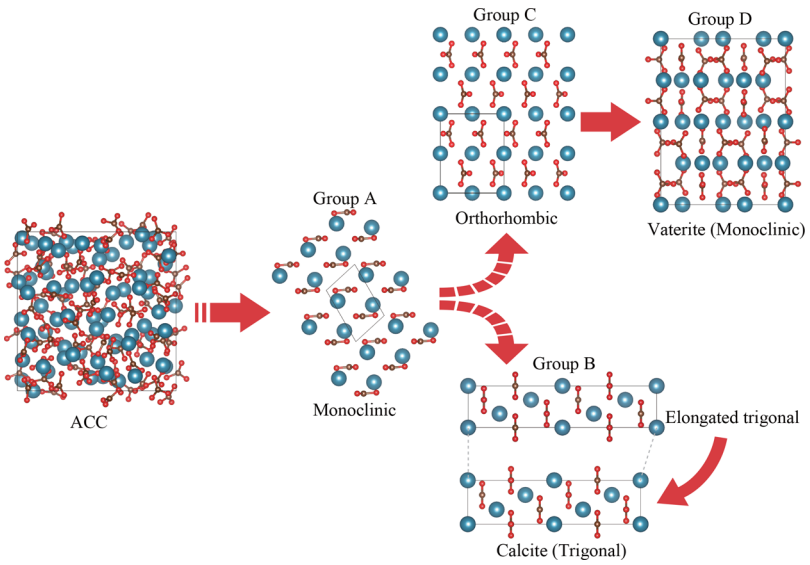

Figure 10. Scenario for generating vaterite crystals while creating symmetric structures from ACC.

structures are unlikely candidates as precursors for vaterite formation. In other words, once CO_3^{2-} layers form within Ca^{2+} sheets, vaterite formation becomes less favorable.

Another set of structures derived from group A is group C, which primarily consists of orthorhombic crystalline systems. From the PES map, group C structures may be generated directly from ACC. These structures result from the rotation of CO_3^{2-} in the interlayer of Ca^{2+} sheets. The formation of either group B or group C from group A may occur with approximately equal probability based on the FES map. The relatively high-energy group-C structures transit to vaterite crystals with $C2/c$ SG in group D. These vaterite structures, with energies approximately 5 kJ/mol higher than that of stable calcite, exhibit lower energy than group-C structures. In real samples, vaterite structures may achieve thermodynamic stabilization due to misfit dislocations, defects, and surface effects.

The intermediate structure for vaterite crystals is group A, and the transition from group A to group C represents a decisive reaction determining the formation of vaterite. Experimentally determined vaterite crystals in group C have been proposed as transition states in DFT studies.[35,45] The crystallization process from hydrated ACC to vaterite via anhydrous ACC has been carefully observed using in situ small- and wide-angle X-ray scattering studies conducted on rapid time scales (seconds).[67] Unfortunately, the intermediate structure of group A detected in this study has not been confirmed through a distinct diffraction pattern. This may be due to its short lifetime, resulting from the instability of the intermediate structure and insufficient crystalline growth. The first step in the conversion of anhydrous ACC to vaterite crystals is the ordering of ACC.[4,68,69] This process is experimentally recognized by broad X-ray peaks and diffraction patterns in the small-angle region.[67,68] The structure of ordering ACC is speculated to be related to the formation of Ca^{2+} sheets, which characterize the group A structure.

These structures should be recognized as intermediates in the transition to $C2/c$ SG, a conclusion supported by this study. It should be noted that the energy differences between the detected structures within the same group are very small, making the transition pathways highly susceptible to exogenous factors such as water and chemical impurities. Natural disorder, such as defects and stacking mismatches observed in real samples, can thermodynamically organize intermediate structures. Although the influence of dehydration and diverse defects in stabilizing intermediate structures cannot be fully captured by WTMetaD simulations alone, the emergence and progression of structural symmetry from ACC represents a universal pathway to vaterite crystalline formation.

5. CONCLUSIONS

Metadynamics simulations of the transition from anhydrous amorphous $CaCO_3$ (ACC) to vaterite crystals were performed using two X-ray diffraction (XRD) peak intensities characteristic of well-known vaterite crystals as collective variables (CVs). Structures sampled as the multiple minima on free energy surface (FES) maps were refined by density functional theory (DFT) calculations, and SGs were determined by examining their symmetry. The determined structures were classified into four groups based on the arrangement of CO_3^{2-} in the interlayer of the Ca^{2+} sheets.

The crystal structures, characterized by CO_3^{2-} lying in the interlayer of Ca^{2+} sheets with monoclinic symmetry, can be considered intermediate structures for the formation of calcite and vaterite crystals. The transition from monoclinic to the stable calcite structure with a trigonal system occurs via metastable states, which exhibit elongation in the stacking direction of Ca^{2+} sheets. Another possible transition route involves the rotation of CO_3^{2-} in the interlayer spaces of Ca^{2+} sheets, producing orthorhombic systems. These structures can be identified as precursors to vaterite with $C2/c$ SG.

A series of phase transitions from ACC to crystalline phases was organized and visualized using subgroup graphs. In real samples, defects, such as surface and stacking mismatches, contribute to the stabilization of intermediate structures as equilibrium states. However, the symmetry-based analysis of the formation mechanism presented in this study provides a guideline for understanding diverse calcium carbonate structures.

https://doi.org/10.1021/acsomega.5c01115
ACS Omega 2025, 10, 17948−17959

■ ASSOCIATED CONTENT

Supporting Information

The Supporting Information is available free of charge at https://pubs.acs.org/doi/10.1021/acsomega.5c01115.

Crystalline structures and SGs of calcite- and vaterite-like structures detected by WTMetaD and refined via DFT calculations (ZIP)

Movie of the time-varying FES with the emergence of sampling points during WTMetaD (movie_FES.mp4) (MP4)

Free energy surface calculated from WTMetaD at 9 and 10.4 μs for convergence check; all crystallographic data (VESTA format[40]) for the derived structures in this study (PDF)

■ AUTHOR INFORMATION

Corresponding Author

Takahiro Ohkubo − *Graduate School of Engineering, Chiba University, Chiba 263-8522, Japan;* orcid.org/0000-0001-8187-1470; Phone: +81 (0)43 2903435; Email: ohkubo.takahiro@faculty.chiba-u.jp; Fax: +81 (0) 43 2903431

Authors

Takumi Saito − *Graduate School of Engineering, Chiba University, Chiba 263-8522, Japan*

Ippei Maruyama − *Department of Architecture, Graduate School of Engineering, The University of Tokyo, Tokyo 113-8656, Japan; Department of Environmental Engineering and Architecture, Graduate School of Environmental Studies, Nagoya University, Nagoya 464-8601, Japan;* orcid.org/0000-0001-7521-3586

Yuya Suda − *Civil Engineering Program, Faculty of Engineering, University of the Ryukyus, Okinawa 903-0213, Japan;* orcid.org/0009-0000-7336-8576

Atsushi Teramoto − *Department of Architecture, Graduate School of Advanced Science and Engineering, Hiroshima University, Hiroshima 739-8527, Japan*

Ryoma Kitagaki − *Division of Human Environmental Systems, Graduate School of Engineering, Hokkaido University, Sapporo 060-8628, Japan*

Complete contact information is available at: https://pubs.acs.org/10.1021/acsomega.5c01115

Notes

The authors declare no competing financial interest.

■ ACKNOWLEDGMENTS

This study was based on the results obtained from a project (JPNP21023) commissioned by the New Energy and Industrial Technology Development Organization (NEDO). The authors thank NEDO for its support. Part of this work was also supported by Japan Society for the Promotion of Science (JSPS) KAKENHI (grant nos. 23H00203 and 23H04096). We acknowledge the ChemRxiv preprint server for providing a platform to share a preprint version of this work(-doi:10.26434/chemrxiv-2025-pxt17).

■ REFERENCES

(1) Hidalgo, A.; Domingo, C.; Garcia, C.; Petit, S.; Andrade, C.; Alonso, C. Microstructural changes induced in Portland cement-based materials due to natural and supercritical carbonation. *J. Mater. Sci.* **2008**, *43*, 3101−3111.

(2) Lu, J.; Ruan, S.; Liu, Y.; Wang, T.; Zeng, Q.; Yan, D. Morphological characteristics of calcium carbonate crystallization in $_2$ pre-cured aerated concrete. *RSC Adv.* **2022**, *12*, 14610−14620.

(3) Steiner, S.; Lothenbach, B.; Proske, T.; Borgschulte, A.; Winnefeld, F. Effect of relative humidity on the carbonation rate of portlandite, calcium silicate hydrates and ettringite. *Cem. Concr. Res.* **2020**, *135*, No. 106116.

(4) Radha, A.; Forbes, T. Z.; Killian, C. E.; Gilbert, P.; Navrotsky, A. Transformation and crystallization energetics of synthetic and biogenic amorphous calcium carbonate. *Proc. Natl. Acad. Sci. U.S.A.* **2010**, *107*, 16438−16443.

(5) Chen, P.; Wang, J.; Wang, L.; Xu, Y.; Qian, X.; Ma, H. Producing vaterite by $_2$ sequestration in the waste solution of chemical treatment of recycled concrete aggregates. *J. Cleaner Prod* **2017**, *149*, 735−742.

(6) Combes, C.; Miao, B.; Bareille, R.; Rey, C. Preparation, physical−chemical characterisation and cytocompatibility of calcium carbonate cements. *Biomaterials* **2006**, *27*, 1945−1954.

(7) Qiao, L.; Feng, Q. Study on twin stacking faults in vaterite tablets of freshwater lacklustre pearls. *J. Cryst. Growth* **2007**, *304*, 253−256.

(8) Kabalah-Amitai, L.; Mayzel, B.; Kauffmann, Y.; Fitch, A. N.; Bloch, L.; Gilbert, P. U.; Pokroy, B. Vaterite crystals contain two interspersed crystal structures. *Science* **2013**, *340*, 454−457.

(9) Jessop, B.; Shiao, J.; Iizuka, Y.; Tzeng, W. Prevalence and intensity of occurrence of vaterite inclusions in aragonite otoliths of American eels Anguilla rostrata. *Aquat. Biol.* **2008**, *2*, 171−178.

(10) Christy, A. G. A review of the structures of vaterite: the impossible, the possible, and the likely. *Cryst. Growth Des.* **2017**, *17*, 3567−3578.

(11) Kamhi, S. R. On the structure of vaterite. *Acta Crystallogr.* **1963**, *16*, 770−772.

(12) Mugnaioli, E.; Andrusenko, I.; Schüler, T.; Loges, N.; Dinnebier, R. E.; Panthöfer, M.; Tremel, W.; Kolb, U. Ab initio structure determination of vaterite by automated electron diffraction. *Angew. Chem., Int. Ed.* **2012**, *51*, 7041−7045.

(13) Okumura, T.; Takahashi, G.; Suzuki, M.; Kogure, T. Stacking Structure of Vaterite Revealed by Atomic Imaging and Diffraction Analysis. *Chem. − Eur. J.* **2024**, *30*, No. e202401557.

(14) San, X.; Hu, J.; Chen, M.; Niu, H.; Smeets, P. J.; Malliakas, C. D.; Deng, J.; Koo, K.; Dos Reis, R.; Dravid, V. P.; et al. Unlocking the mysterious polytypic features within vaterite. *Nat. Commun.* **2023**, *14*, 7858.

(15) De La Pierre, M.; Demichelis, R.; Wehrmeister, U.; Jacob, D. E.; Raiteri, P.; Gale, J. D.; Orlando, R. Probing the multiple structures of vaterite through combined computational and experimental Raman spectroscopy. *J. Phys. Chem. C* **2014**, *118*, 27493−27501.

(16) Burgess, K. M.; Bryce, D. L. On the crystal structure of the vaterite polymorph of $_3$: A calcium-43 solid-state NMR and computational assessment. *Solid State Nucl. Magn. Reson.* **2015**, *65*, 75−83.

(17) Beniash, E.; Aizenberg, J.; Addadi, L.; Weiner, S. Amorphous calcium carbonate transforms into calcite during sea urchin larval spicule growth. *Proc. R. Soc. London, Ser. B* **1997**, *264*, 461−465.

(18) Dillaman, R.; Hequembourg, S.; Gay, M. Early pattern of calcification in the dorsal carapace of the blue crab Callinectes sapidus. *J. Morphol.* **2005**, *263*, 356−374.

(19) Marxen, J. C.; Becker, W.; Finke, D.; Hasse, B.; Epple, M. Early mineralization in Biomphalaria glabrata: microscopic and structural results. *J. Phys. Chem. C* **2003**, *69*, 113−121.

(20) Uno, T.; Saeki, N.; Maruyama, I.; Suda, Y.; Teramoto, A.; Kitagaki, R.; Ohkubo, T. Understanding the Carbonation Phenomenon of C−S−H through Layer Structure Changes and Water Exchange. *J. Phys. Chem. C* **2024**, *128*, 11802−11816.

(21) Addadi, L.; Raz, S.; Weiner, S. Taking advantage of disorder: amorphous calcium carbonate and its roles in biomineralization. *Adv. Mater.* **2003**, *15*, 959−970.

(22) Gago-Duport, L.; Briones, M.; Rodríguez, J.; Covelo, B. Amorphous calcium carbonate biomineralization in the earthworm's calciferous gland: pathways to the formation of crystalline phases. *J. Struct. Biol.* **2008**, *162*, 422−435.
(23) Saeki, N.; Kurihara, R.; Ohkubo, T.; Teramoto, A.; Suda, Y.; Kitagaki, R.; Maruyama, I. Semi-dry natural carbonation at different relative humidities: Degree of carbonation and reaction kinetics of calcium hydrates in cement paste. *Cem. Concr. Res.* **2025**, *189*, No. 107777.
(24) Cartwright, J. H.; Checa, A. G.; Gale, J. D.; Gebauer, D.; Sainz-Díaz, C. I. Calcium carbonate polyamorphism and its role in biomineralization: how many amorphous calcium carbonates are there? *Angew. Chem., Int. Ed.* **2012**, *51*, 11960−11970.
(25) Du, H.; Amstad, E. Water: How does it influence the $_3$ formation? *Angew. Chem. Int. Ed* **2020**, *59*, 1798−1816.
(26) Tsao, C.; Yu, P.-T.; Lo, C.-H.; Chang, C.-K.; Wang, C.-H.; Yang, Y.-W.; Chan, J. C. C. Anhydrous amorphous calcium carbonate (ACC) is structurally different from the transient phase of biogenic ACC. *Chem. Commun.* **2019**, *55*, 6946−6949.
(27) Politi, Y.; Metzler, R. A.; Abrecht, M.; Gilbert, B.; Wilt, F. H.; Sagi, I.; Addadi, L.; Weiner, S.; Gilbert, P. Transformation mechanism of amorphous calcium carbonate into calcite in the sea urchin larval spicule. *Proc. Natl. Acad. Sci. U. S. A.* **2008**, *105*, 17362−17366.
(28) Gong, Y. U.; Killian, C. E.; Olson, I. C.; Appathurai, N. P.; Amasino, A. L.; Martin, M. C.; Holt, L. J.; Wilt, F. H.; Gilbert, P. Phase transitions in biogenic amorphous calcium carbonate. *Proc. Natl. Acad. Sci. U. S. A.* **2012**, *109*, 6088−6093.
(29) Gebauer, D.; Volkel, A.; Colfen, H. Stable prenucleation calcium carbonate clusters. *Science* **2008**, *322*, 1819−1822.
(30) Tomono, H.; Nada, H.; Zhu, F.; Sakamoto, T.; Nishimura, T.; Kato, T. Effects of magnesium ions and water molecules on the structure of amorphous calcium carbonate: A molecular dynamics study. *J. Phys. Chem. B* **2013**, *117*, 14849−14856.
(31) Nada, H.; Nishimura, T.; Sakamoto, T.; Kato, T. Heterogeneous growth of calcite at aragonite {001}-and vaterite {001}-melt interfaces: A molecular dynamics simulation study. *J. Cryst. Growth* **2016**, *450*, 148−159.
(32) Demichelis, R.; Raiteri, P.; Gale, J. D.; Dovesi, R. The multiple structures of vaterite. *Cryst. Growth Des.* **2013**, *13*, 2247−2251.
(33) Demichelis, R.; Raiteri, P.; Gale, J. D.; Quigley, D.; Gebauer, D. Stable prenucleation mineral clusters are liquid-like ionic polymers. *Nat. Commun.* **2011**, *2*, 590.
(34) Shuseki, Y.; Kohara, S.; Ohara, K.; Ohkubo, T.; Takei, K.; Tucker, M. G.; Kolesnikov, A. I.; McDonnell, M. T.; Sacci, R. L.; Neuefeind, J. C.; et al. Structural analyses of amorphous calcium carbonate before and after removing strontium ions from an aqueous solution. *J. Ceram. Soc. Jpn.* **2022**, *130*, 225−231.
(35) Demichelis, R.; Raiteri, P.; Gale, J. D.; Dovesi, R. A new structural model for disorder in vaterite from first-principles calculations. *CrystEngComm* **2012**, *14*, 44−47.
(36) Medeiros, S.; Albuquerque, E.; Maia, F., Jr; Caetano, E.; Freire, V. First-principles calculations of structural, electronic, and optical absorption properties of $CaCO_3$ Vaterite. *Chem. Phys. Lett.* **2007**, *435*, 59−64.
(37) Zhu, X.; Dupuis, R.; Pellenq, R. J.-M.; Ioannidou, K. Collective molecular-scale carbonation path in aqueous solutions with sufficient structural sampling: From CO_2 to $CaCO_3$. *J. Chem. Phys.* **2024**, *161*, 184502.
(38) Lodesani, F.; Menziani, M. C.; Urata, S.; Pedone, A. Evidence of multiple crystallization pathways in lithium disilicate: a metadynamics investigation. *J. Phys. Chem. Lett.* **2023**, *14*, 1411−1417.
(39) Togo, A.; Shinohara, K.; Tanaka, I. Spglib: a software library for crystal symmetry search. *Sci. Technol. Adv. Mater. Methods* **2024**, *4*, No. 2384822.
(40) Momma, K.; Izumi, F. VESTA: a three-dimensional visualization system for electronic and structural analysis. *J. Appl. Crystallogr.* **2008**, *41*, 653−658.
(41) Barducci, A.; Bussi, G.; Parrinello, M. Well-tempered metadynamics: a smoothly converging and tunable free-energy method. *Phys. Rev. Lett.* **2008**, *100*, No. 020603.
(42) Warren, B. *X-ray Diffraction*; Dover, 1990; vol *208*.
(43) Lorch, E. Neutron diffraction by germania, silica and radiation-damaged silica glasses. *J. Phys. C Solid State Phys.* **1969**, *2*, 229.
(44) Le Bail, A.; Ouhenia, S.; Chateigner, D. Microtwinning hypothesis for a more ordered vaterite model. *Powder Diffr.* **2011**, *26*, 16−21.
(45) Meyer, H. J. Ueber Vaterit und seine Struktur. *Fortschr. Mineral.* **1960**, *38*, 186−187.
(46) Plimpton, S. Fast Parallel Algorithms for Short-Range Molecular Dynamics. *J. Comput. Phys.* **1995**, *117*, 1−19.
(47) PLUMED consortium. Promoting transparency and reproducibility in enhanced molecular simulations. *Nat. Methods* **2019**, *16*, 670−673.
(48) Raiteri, P.; Demichelis, R.; Gale, J. D. Thermodynamically consistent force field for molecular dynamics simulations of alkaline-earth carbonates and their aqueous speciation. *J. Phys. Chem. C* **2015**, *119*, 24447−24458.
(49) Raiteri, P.; Schuitemaker, A.; Gale, J. D. Ion pairing and multiple ion binding in calcium carbonate solutions based on a polarizable AMOEBA force field and ab initio molecular dynamics. *J. Phys. Chem. B* **2020**, *124*, 3568−3582.
(50) Dasgupta, N.; Chen, C.; Van Duin, A. C. Development and application of ReaxFF methodology for understanding the chemical dynamics of metal carbonates in aqueous solutions. *Phys. Chem. Chem. Phys.* **2022**, *24*, 3322−3337.
(51) Kayano, R.; Inagaki, Y.; Matsubara, R.; Ishida, K.; Ohkubo, T. Development and Validation of Neural Network Potentials for Multicomponent Oxide Glasses. *J. Phys. Chem. C* **2024**, *128*, 17686−17702.
(52) Evans, D. J.; Holian, B. L. The nose−hoover thermostat. *J. Chem. Phys.* **1985**, *83*, 4069−4074.
(53) Lodesani, F.; Menziani, M. C.; Urata, S.; Pedone, A. Biasing crystallization in fused silica: An assessment of optimal metadynamics parameters. *J. Chem. Phys.* **2022**, *156*, 194501.
(54) Hafner, J. Ab-initio simulations of materials using VASP: Density-functional theory and beyond. *J. Comput. Chem.* **2008**, *29*, 2044−2078.
(55) Kresse, G.; Hafner, J. Ab initio molecular dynamics for liquid metals. *Phys. Rev. B* **1993**, *47*, 558.
(56) Kresse, G.; Furthmüller, J. Efficient iterative schemes for ab initio total-energy calculations using a plane-wave basis set. *Phys. Rev. B* **1996**, *54*, 11169.
(57) Perdew, J. P.; Ruzsinszky, A.; Csonka, G. I.; Vydrov, O. A.; Scuseria, G. E.; Constantin, L. A.; Zhou, X.; Burke, K. Restoring the density-gradient expansion for exchange in solids and surfaces. *Phys. Rev. Lett.* **2008**, *100*, No. 136406.
(58) Gavryushkin, P. N.; Belonoshko, A. B.; Sagatov, N.; Sagatova, D.; Zhitova, E.; Krzhizhanovskaya, M. G.; Recnik, A.; Alexandrov, E. V.; Medrish, I. V.; Popov, Z., I; et al. Metastable structures of $_3$ and their role in transformation of calcite to aragonite and postaragonite. *Cryst. Growth Des* **2021**, *21*, 65−74.
(59) Graf, D. L. Crystallographic tables for the rhombohedral carbonates: A correction. *Am. Mineral.* **1969**, *54*, 325−325.
(60) Antao, S. M.; Hassan, I.; Mulder, W. H.; Lee, P. L.; Toby, B. H. In situ study of the orientational disorder in calcite. *Phys. Chem. Miner.* **2009**, *36*, 159−169.
(61) Liu, J.; Duan, C.-G.; Ossowski, M.; Mei, W.; Smith, R.; Hardy, J. Simulation of structural phase transition in $_3$ and. *Phys. Chem. Miner* **2001**, *28*, 586−590.
(62) Müller, U.; Wondratschek, H. *International Tables for Crystallography Vol. A1: Symmetry relations between space groups*, 2nd online ed. ed.; Wiley, 2006.
(63) Aroyo, M. I.; Perez-Mato, J. M.; Capillas, C.; Kroumova, E.; Ivantchev, S.; Madariaga, G.; Kirov, A.; Wondratschek, H. Bilbao Crystallographic Server: I Databases and crystallographic computing programs. *Z. Kristallogr. - Cryst. Mater.* **2006**, *221*, 15−27.

https://doi.org/10.1021/acsomega.5c01115
ACS Omega 2025, 10, 17948−17959

(64) Aroyo, M. I.; Kirov, A.; Capillas, C.; Perez-Mato, J.; Wondratschek, H. Bilbao Crystallographic Server. II. Representations of crystallographic point groups and space groups. *Acta Crystallogr., Sect. A: Found. Crystallogr.* **2006**, *62*, 115−128.
(65) Ivantchev, S.; Kroumova, E.; Madariaga, G.; Pérez-Mato, J.; Aroyo, M. SUBGROUPGRAPH: a computer program for analysis of group−subgroup relations between space groups. *J. Appl. Crystallogr.* **2000**, *33*, 1190−1191.
(66) Steciuk, G.; Palatinus, L.; Rohlíček, J.; Ouhenia, S.; Chateigner, D. Stacking sequence variations in vaterite resolved by precession electron diffraction tomography using a unified superspace model. *Sci. Rep.* **2019**, *9*, 9156.
(67) Bots, P.; Benning, L. G.; Rodriguez-Blanco, J.-D.; Roncal-Herrero, T.; Shaw, S. Mechanistic insights into the crystallization of amorphous calcium carbonate (ACC). *Cryst. Growth Des.* **2012**, *12*, 3806−3814.
(68) Rodriguez-Blanco, J. D.; Shaw, S.; Benning, L. G. The kinetics and mechanisms of amorphous calcium carbonate (ACC) crystallization to calcite, via vaterite. *Nanoscale* **2011**, *3*, 265−271.
(69) Navrotsky, A. Energetic clues to pathways to biomineralization: Precursors, clusters, and nanoparticles. *Proc. Natl. Acad. Sci. U.S.A.* **2004**, *101*, 12096−12101.

https://doi.org/10.1021/acsomega.5c01115
ACS Omega 2025, 10, 17948−17959